XPS fast depth profile of the native oxide layers on AISI 304, 316 and 430 commercial stainless steels and their evolution with time

Detriche, Simon; Vivegnis, Sebastien; Vanhumbeeck, Jean-François; Felten, Alexandre; Louette, Pierre; Renner, Frank; DELHALLE, Joseph; MEKHALIF, Zineb

Published in:
Journal of Electron Spectroscopy and Related Phenomena

DOI:
10.1016/j.elspec.2020.146970

Publication date:
2020

Document Version
Peer reviewed version

Journal Pre-proof

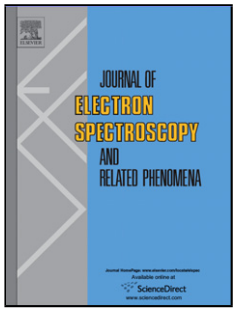

XPS fast depth profile of the native oxide layers on AISI 304, 316 and 430 commercial stainless steels and their evolution with time

S. Detriche, S. Vivegnis, J.-F. Vanhumbeeck, A. Felten, P. Louette, F.U. Renner, J. Delhalle, Z. Mekhalif

PII: S0368-2048(20)30038-4

DOI: https://doi.org/10.1016/j.elspec.2020.146970

Reference: ELSPEC 146970

To appear in: *Journal of Electron Spectroscopy and Related Phenomena*

Received Date: 23 July 2019

Revised Date: 26 May 2020

Accepted Date: 28 May 2020

Please cite this article as: Detriche S, Vivegnis S, Vanhumbeeck J-F, Felten A, Louette P, Renner FU, Delhalle J, Mekhalif Z, XPS fast depth profile of the native oxide layers on AISI 304, 316 and 430 commercial stainless steels and their evolution with time, *Journal of Electron Spectroscopy and Related Phenomena* (2020), doi: https://doi.org/10.1016/j.elspec.2020.146970

XPS fast depth profile of the native oxide layers on AISI 304, 316 and 430 commercial stainless steels and their evolution with time

S. Detriche[1], S. Vivegnis[1,4,5], J.-F. Vanhumbeeck[3], A. Felten[2], P. Louette[2], F.U. Renner[4,5], J. Delhalle[1] and Z. Mekhalif[1]

[1] Laboratory of Chemistry and Electrochemistry of Surfaces (CES), Namur Institute for Structured Matter (NISM), University of Namur, rue de Bruxelles, 61, B-5000 Namur, Belgium

[2] Synthesis, Irradiation & Analysis of Materials (SIAM), University of Namur, rue de Bruxelles, 61, B-5000 Namur, Belgium

[3]Centre de Recherches Métallurgiques (CRM), Avenue du Bois Saint-Jean 21, B27 – Quartier Polytech 4, B-4000 Liège, Belgium

[4] Institute for Materials Research (IMO), Hasselt University, B-3590 Diepenbeek, Belgium

[5] IMEC vzw. Division IMOMEC, 3590 Diepenbeek, Belgium

Abstract

The thin oxide layers forming on the metal surfaces of metals determine their interactions with the environment and have a strong influence on the materials properties such as corrosion resistance. Such oxide layers typically have a thickness in the range of a few nanometres, which is a challenge for the analysis of their chemical nature and structure. To characterize such materials and surfaces, XPS using depth profile sputtering is a sensitive and powerful technique. However, it is rather elaborate and raises the risk of changing the nature of the surface layer during the analysis process. This work reports on a protocol for a faster approach to depth profile X-Ray photoelectron spectroscopy (XPS) analysis to obtain accurate and reproducible information on the oxide layer structure by using the snapshot mode of the XPS instrument. This protocol is applied to three stainless steels differing by their chemical composition: FeCr AISI 430, FeCrNi AISI 304 and the chemically more complex FeCrNiMo AISI 316. The respective oxide layer structures observed using this methodology are consistent with literature data. In addition, the structures have been confirmed using non-destructive techniques such as angle-resolved XPS (AR-XPS) and Hard XPS (HAXPES). Finally, the analysis protocol has been applied

to obtain information on the evolution of the surface chemistry of those stainless steel grades resulting from mechanical polishing and subsequent aging in contact with atmosphere.

Keywords: XPS; Evolution with time; fast depth profile; Oxide layer structure; stainless steel; polishing

I. Introduction

Today, stainless steels are widely used materials in various applications such as architecture, construction, automotive, transportation, medical, energy and heavy industries [1]. The overall world production of stainless steel in 2017 was 48 million tons with a 5% yearly increase [2]. The wide use of such materials is due to their excellent physical and mechanical properties, versatility and corrosion resistance [3]. Corrosion resistance stems from the presence of a chromium rich oxide layer on the surface acting as a diffusion barrier for iron and chromium ions [4]. The oxide layers of stainless steels are only a few nanometers thin [5,6] and their composition and structure strongly depend on the bulk composition and the elaboration processes [7–9]. Therefore, the formation and structure of the oxide layers as well as the role of the alloying elements have to be investigated to better understand the corrosion resistance of stainless steels. Coarse-grinded surfaces and polishing of different grades are of interest for applications.

In the past decades, several studies have been devoted to the knowledge of the stainless steels oxide layers mostly using surface analysis techniques: ISS (Ion-Scattering Spectrometry), XPS (X-Ray Photoelectron Spectroscopy), AR-XPS (Angle-Resolved X-ray Photoelectron Spectroscopy), HAX-PES (High energy X-ray photoelectron spectroscopy), HAR-XPS (High energy Angle-Resolved X-ray Photoelectron Spectroscopy) and AES (Auger Electron Spectroscopy) [5,7,10–12]. These techniques can be classified into non-destructive (AR-XPS, HAX-PES and HAR-XPS) and destructive ones (AES and XPS depth profile). The later can lead to preferential etchings [8,12]. In the case of stainless steels, both types of techniques provide generally similar results [6]. TEM and SEM studies have proved that stainless steels are quite homogenous in term of the elements lateral distribution [13]. Accordingly, there will be no negative consequence due to the large analysis spot area of the XPS. The various technical approaches proposed in the literature present drawbacks such as (i) costly equipment (HAX-PES), (ii) analysis limited to extreme surface features (AR-XPS, XPS, AES) or (iii) time-consuming analysis in the case of AES and XPS depth profile using the scan acquisition mode.

Many details about the oxide layer structure of stainless steels have been reported in the literature using these approaches [5–8,10–12]. Features of the oxide layer depend on the presence of some alloying elements like nickel and molybdenum. Three main observations can be highlighted from the literature about the natively formed oxide layer onto different steel surfaces: (i) the presence of a layer rich in chromium oxide beneath a surface layer rich in iron oxide. (ii) For nickel-containing stainless steels, the presence of a layer rich in metallic nickel between the oxide layer and the bulk. (iii) For the molybdenum containing stainless steels, there is a lack of agreement about the role of molybdenum in the oxide layer.

There is a consensus in the literature about the presence of at least two layers in the oxide structure natively formed on steel surfaces, with an external iron-rich layer and an internal chromium-rich one. This result has been confirmed using non-destructive methods such as HAXPES [14], AR-XPS [14], inelastic electrons background analysis [15], ion scattering spectroscopy [6,16] and analysis of the XPS signal [8,11,17]. Confirmation of the structure has also been obtained using comparison between XPS and SXPS (Soft-XPS, as the use of various X-ray energies allows the emission, for the same metal, of photoelectrons with various energies and thus various mean free paths) [18] on different steels including AISI 316 and 304. Similar results have also been obtained using destructive methods like AES and XPS depth profile [5,7,19–21]. The precise nature of this layer is still to be investigated. Some authors suggest a “chromium rich” layer [5,16,20] and others clearly point to a a Cr_2O_3 layer [15,18,19,21]. The formation of this chromium-rich layer is usually interpreted as a consequence of easier iron ions diffusion or migration to the surface [5,15]. However, as stated by Calinski *et al.* [16], the oxide layers structure also depends on the preferential dissolution and diffusion of iron and/or chromium in the electrolytes. This can account for the fact that in some conditions, the oxide layer consists only of chromium oxide. It is worth noticing that a trilayer model of the oxide layer, with an intermediate iron/chromium oxide layer has been suggested by Lince [18].

For nickel-containing stainless steels, the presence of an accumulation of metallic nickel between the external oxide layer and the bulk has been widely reported in the literature. This has been demonstrated by using destructive methods of analysis such as AES and XPS depth profile [5,7,21–23], as well as by non-destructive methods such as electron background analysis [15] AR-XPS and HAXPES [14] or HIKPES (High Kinetic Energy Photo Electron Spectroscopy) [24]. The reason usually given for this accumulation is the lower oxidation ability of nickel compared to chromium and iron. The absence of detectable nickel oxide in the oxide layer is also reported [5,7,14,15,21–24]. This absence of oxide can originate from a higher solubility in most electrolytes of the nickel ions compared to iron and chromium ions.

In the case of molybdenum containing stainless steels, some authors report the presence of molybdenum oxide throughout all the oxide layer (Fredrikson [14], on AISI 316) while others point to the absence of molybdenum in the oxide layer [7,12,25]. A similar observation can be made concerning the presence of a molybdenum accumulation beneath the oxide layer [19,25]. Interestingly, in a stainless steel (Duplex 2205) containing molybdenum nickel accumulation is not observed beneath the oxide layer [26]. However, an accumulation of nickel and molybdenum beneath the oxide layer is observed on other steels. Its presence is related to the potential at which the samples have been polarized [27]. Hence, more investigations are needed since the oxide layer of these complex stainless steels appears strongly dependent on the analysis conditions.

Concerning the stability of the oxide layers, Olsson *et al.* [5] stated that the small thickness of the oxide layer makes it a fast-adaptating system in equilibrium with its environment. Accordingly, some authors [6,8, 28] pay attention to the preparation time of their samples and the time delay until the analysis. The influence of preparation conditions (time, polarization…) has already been reported [7,8] where the process appears to take hours. In order to further clarify this point, a study of the influence of the resting time after mechanical polishing has been considered in this work.

In this contribution, several points are developed: (i) a methodology for a fast XPS analysis of thin oxide layers on stainless steels based on a fast depth profiling, (ii) a mathematical treatment to determine the oxide layer structure, (iii) a morphology study of the oxide layer of the as-received and mechanically polished stainless steel samples (iv) their evolution with atmosphere exposure time and (v) a comparison of the obtained structures with those acquired using non-destructives methods (AR-XPS and HAXPES).

II. Experimental

II.1. Preparation of reference samples for etching rate calibration

Pure Cr and Fe samples are analyzed, during etching with Ar ions, in order to remove impurities and to set up a mathematical and physically meaningful fit for these elements

In order to calibrate chromium and iron etching speeds, reference samples (Cr_{ref} and Fe_{ref}) have been prepared by plasma vapor deposition (Quorum Q150T ES) using 99.95 % pure chromium (Neyco) and 99.95 % pure iron (Ted Pella) sources. A quartz-crystal microbalance is coupled with the PVD system, to measure the thickness of the sputtered materials. On a mirror polished AISI 316L substrate, successive layers of chromium (or iron) with different thicknesses (5, 10 and 15 nm) have been elaborated by sputtering. Between the formation steps of each layer, a spontaneous chromium (or

iron) oxide layer forms by contact with the atmosphere during 60 seconds. The Cr and Fe standards are analysed by depth-profile XPS to measure the etching speed of these elements.

II.2. Modification of the native oxide layer

Three commercial stainless steels (AISI 304, 316 and 430) are studied to assess their oxide layer structure. Their bulk composition (AISI norms) is provided in Table 1. Those steels have been selected for their increasing composition complexity. As received samples exhibit a polished and a grinded side (Figure 1). The grinded side, referred to "as-received", is the one often used in industrial applications requiring non–polished stainless steels and consequently will be the one of interest in this work. The grinded surface presents a repetitive linear structuration along the grinding axis. Therefore, two sets of roughness parameters are measured per sample: one parallel and the other perpendicular to the grinding axis (Table 1). A Mitutoyo SJ-210 apparatus is used to measure the roughness parameter (Ra) according to the ISO-4288 norm. An arithmetic mean is calculated based on twelve measurements of Ra performed on each sample, both in a parallel and perpendicular directions with respect to the grinding axis.

Figure 1: A representative as-received sample (2 cm in length), with polished (left) and a grinded side (right)

Element	AISI 430	AISI 304	AISI 316
Fe	81.7 to 82.7	68.4 to 72.1	62.8 to 69.6
Cr	16.3 to 17.3	18.4 to 20.2	17.7 to 19.5
Ni	-	7.4 to 9.4	9.5 to 12.1
Mo	-	-	1.2 to 1.4
Mn	1.0	< 2.0	2.0
Ra (µm) parallel	0.258 ± 0.080	0.197 ± 0.067	0.529 ± 0.142
Ra (µm) perpendicular	0.575 ± 0.025	0.774 ± 0.093	0.919 ± 0.049

Table 1: AISI norm bulk composition (atomic percentages) and roughness (parallel and perpendicular to the grinding axis) for the three studied stainless steels

In the second part of the work, the grinded sides of AISI 304, 316 and 430 samples are mechanically polished using a Buehler Ecomet 300. They are first polished using silicon carbide papers (180, 300, 800 and 1200 granulometry grid) and milliQ water as lubricant, then with commercial water-based suspensions of diamond (9, 3 and 1 µm). At the end of the polishing steps, the samples exhibit a uniform and mirror-like appearance without visible defects or scratches. After polishing, the samples

are thoroughly washed with ethanol, sonicated 15 min in ethanol and dried in a nitrogen flow. The measured roughness (Ra) after polishing with the diamond suspension is less than 0.010 microns, which corresponds to the detection limit of the Mitutoyo SJ-210 profilometer.

Native oxide layer aging of the grinded sides of these stainless steels has also been studied. Technically, samples are polished down to mirror appearance and analysed just after the polishing steps, then stored in contact with air during 24, 48, 72, 210 and 384 hours after the last polishing step prior to XPS surface and depth profile analyses.

II.3. XPS surface and depth-profile analyses

XPS surface and depth profile analyses are performed with a Thermo Scientific K-Alpha spectrometer (1486.61 eV X-Ray source). Depth profiling is performed by Ar^+ (500 eV kinetic energy) sputtering. The pressure in the analysis chamber is ~ 5 x 10^{-8} mbar. The sputtered surface area is 1 mm^2 and the analyzed area (200 x 150 µm) is of elliptic form. The depth profile analysis consists in 20 sputtering steps of 1 s followed by 10 sputtering steps of 5 s. After each sputtering step, a snapshot acquisition for each element was performed [28]. In this acquisition mode, the photoelectrons are recorded in parallel with 128 channeltrons, without scanning in an energy range. This acquisition mode is fast, but must be used with a high pass energy (150 eV), which decreases the resolution in energy. In order to reduce surface effects and be more bulk sensitive, photoelectrons are collected at 0° with respect to the surface normal using a hemispherical analyser. The Smart Background option of the Thermo Avantage software is used to measure the peaks area and is based on the Shirley Background with the additional constraint that the background is not allowed to have a higher intensity than the actual data for any point in the analysed region [29].

II.4. Complementary analyses by non-destructive methods

Both angle-resolved XPS (AR-XPS) and Hard XPS (HAXPES) have been used as non-destructive methods to study the oxide layer structures and thereby validate our XPS depth profile analyses.

AR-XPS measurements were performed with a Thermo Scientific K-alpha spectrometer, recording the data while tilting the substrate from 0.0 to 80.0° by 4.2° steps. Prior to AR-XPS measurement, a soft etching using Ar^+ beam (500 eV) on a large sputtering surface (4 mm^2) has been used to remove the carbonaceous impurities without damaging the oxide layer. The snapshot acquisition mode was used, as explained above.

HAXPES measurements were performed at the Galaxies beamline, Soleil Synchrotron, using a EW4000 Scienta hemispherical electron analyzer oriented at 90° with respect to the incident photon beam and collinear to the horizontal polarization axis [30,31]. The usual pressure inside the analysis chamber is

in the range of 1 to 3 x 10^{-9} mbar. The beamline energy is tuned by adjusting the Bragg angle of the cryogenically cooled double-crystal monochromator (DCM). For the present experiment, the first order reflexion of the Si(111) crystal of the DCM was used for the 2.3keV photon energy, whereas the third order reflexion of the DCM was used to select the 6.9keV photon energy. The corresponding resolutions are ~200meV and ~150meV, respectively. The photon beam grazing incidence is 5° with respect to the surface. Energy calibration was performed using the Au4f7/2 spectral line at 84.0 eV binding energy. The HAXPES data were analyzed using the Casa software, a Shirley background and the common Scofield sensitivity factors.

II.5: Determination of the oxide layer structure based on the Strohmeier equation

Strohmeier [32] established a formula to determine the thickness of an oxide layer using the metallic and oxide components of the XPS signal,

$$d = \lambda_o * \sin\theta * \ln\left[\frac{N_m * \lambda_m * I_o}{N_o * \lambda_o * I_m} + 1\right]$$

In this equation, d is the oxide layer thickness (Å), N_o and N_m the densities of the metal atoms in the oxide and metallic states, respectively, θ the electron take-off angle (with respect to the sample surface), I_o and I_m the peak area of the oxide and the metal, respectively, and λ_o and λ_m the inelastic mean free path (IMFP) of electrons in the oxide and the metal, respectively.

The Strohmeier formula implies a homogeneous oxide layer and requires the decomposition of the XPS signal into the metallic and oxide components. Using a similar approach, Lince *et al.* [18] obtained different oxide layers thickness for the same sample depending on the use of iron or chromium signal. They interpreted this as the result of a depletion in iron at the vicinity of the oxide-metal interface.

In this paper, we propose a new application of the Strohmeier formula adapted to depth profiles. The novelty of our approach is to apply the formula to each step of the depth profiling. The measured (residual) thickness $d(t)$ is expected to be related to the initial thickness d_0 and to the etching rate $\varepsilon_R(t)$ as expressed in the equation below:

$$d(t) = d_0 - \int \varepsilon_R(t)dt$$

In the presence of a uniform oxide layer, the etching rate is constant hence leading to a linear decrease of the calculated thickness, the slope corresponding to the etching speed. In the case of a bilayered oxide, the plot of residual oxide thickness versus etching time should present two different consecutive

slopes, giving information on the change in composition and the respective thickness of each layer of the oxide.

III. Results

III.1. Standard materials characterization

III.1.1. Fitting parameters for the iron signal

To establish a table with fitting parameters for the Fe2p3/2 signal, a mirror-like polished pure iron sample was analysed by depth-profile XPS. The depth profile evolution of the C1s, Fe2p and O1s peaks is presented in Figure 2.

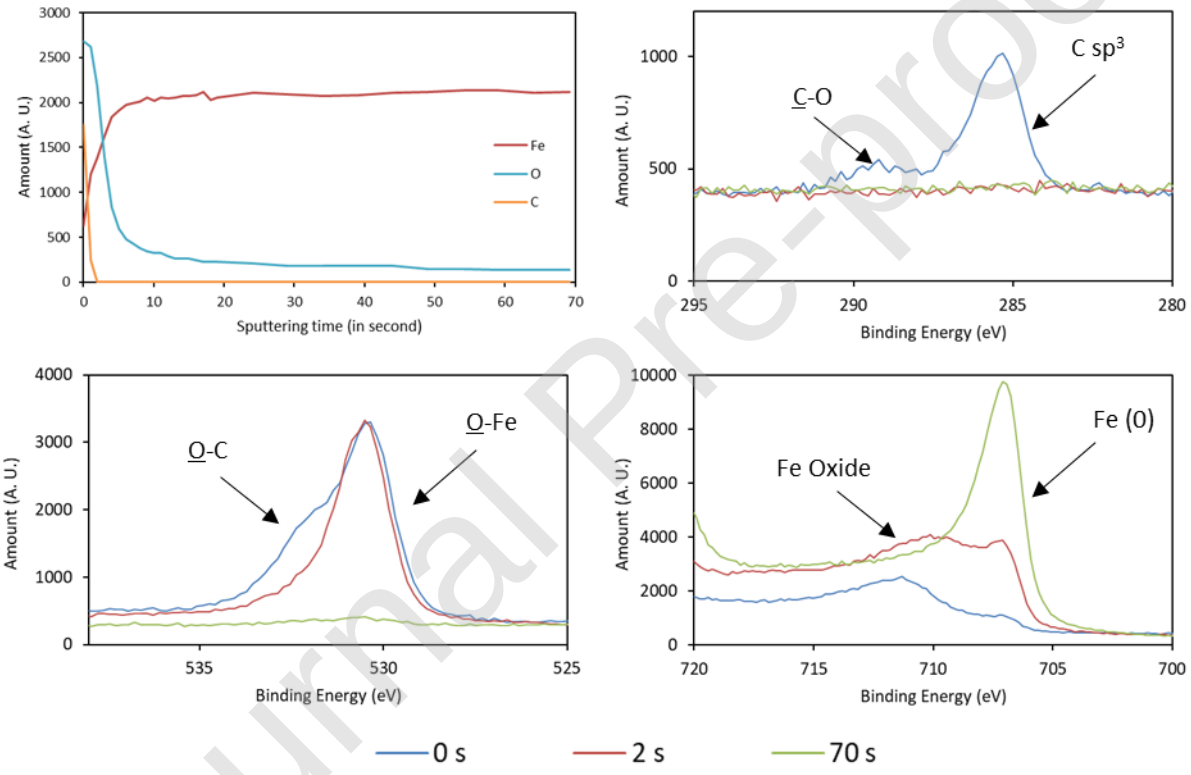

Figure 2: Evolution of the amount of carbon, oxygen and iron contents during the depth profiling of mirror-polished pure iron surface (a) and the evolution of the Fe2p3/2 (b), C1s (c) and O1s (d) spectra.

Carbon is only detected at the extreme surface of the sample. The oxygen content swiftly decreases with etching time even if some traces of oxygen can still be detected after 70 seconds of etching. This presence of oxygen at larger depths is possibly originating from the edge of the sputtering site or from the residual roughness of the sample, which protects some oxygenated species from the etching.

From the evolution of the O1s spectra (figure 2), it is clear that on the two first levels of the depth profile, the O1s peak at 533.3 eV corresponds to oxygen linked to carbon whose components appear at 286.0 and 289.0 eV in the C1s spectra [33]. After the removal of carbon by etching, the residual oxygen components at 530.2 and 531.3 eV only correspond to iron oxides and hydroxides, respectively [34].

The components corresponding to oxidized forms of iron are determined on the basis of the Fe2p3/2 signal before etching, using parameters from the literature [35–37] and adapted to the lower resolution of our instrument and to the use of a snapshot acquisition mode. Consequently, the components of the multiplet corresponding to oxidized iron cannot be distinguished. In addition, the overlap of the various components of the different oxidized species makes the fitting almost impossible [37]. The only distinguishable feature is the first component of the Fe (II) multiplet, because it has a significantly different binding energy than both Fe (0) and Fe (III). The fitting parameters for Fe2p3/2 signal used in the present work are shown on Table 3. Since almost no oxygen is detected at the last stage of the depth profile, the asymmetric components of the metallic Fe (Fe2p3/2) signal is the only one detected and which allows the extraction of their asymmetry parameters.

Component	Binding energy (eV)	FWHM (eV)
Metallic Fe, 1st component	706.6	1.2
Metallic Fe, 2nd component	707.4	1.2
Fe (II) oxide, 1st component	708.4	1.5
Fe (II) and Fe (III) mixed, 1st component	709.8	2.0
Fe (II) and Fe (III) mixed, 2nd component	711.3	2.0
Fe (II) and Fe (III) mixed, 3rd component	712.5	2.0
Fe (II) and Fe (III) mixed, 4th component	714.2	2.0
Siderite ($FeCO_3$)	715.6	2.0

Table 2: Fitting parameters used for the Fe2p3/2 signal

By using these fitting parameters for the depth profile realized on pure iron, the amount of oxygen (from the O1s peak) matches the amount of oxygen linked to iron (oxidized iron from the Fe2p3/2 peak), as shown in figure 3.

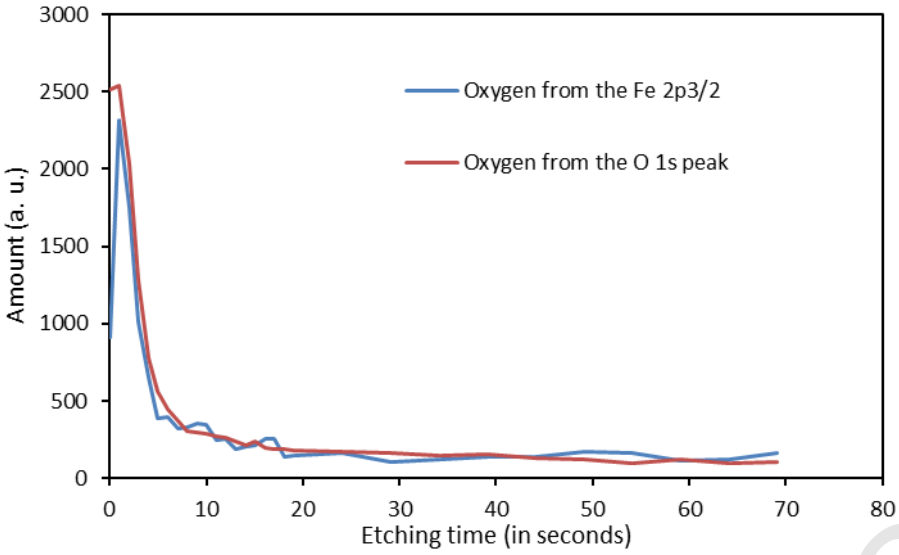

Figure 3: Evolution of the oxygen content calculated from the O1s and Fe2p3/2 peaks

III.1.2. Fitting parameters for the chromium signal

Following the same procedure as for iron, the fitting parameters for Cr2p3/2 (Table 4) are established by analyzing pure chromium layers. For chromium (III), the corresponding oxide and hydroxide species exhibit two components which appear as overlapping multiplets (figure 1 in [37]). The first component of the oxide peak is characterized by a lower binding energy than the one corresponding to the hydroxide peak and therefore can be used to estimate the amount of Cr (III) oxide and consequently that of Cr (III) hydroxide. Chromium (VI), in oxide or hydroxide forms, arises at a higher binding energy and appears as a single peak.

Cr 2p3/2 components	Binding energy (eV)	FWHM (eV)
Metallic Cr	574.3	1.5
Cr (III) oxide, first component	575.8	2.0
Cr (III) hydroxide and other components of Cr (III) oxide	577.4	2.0
Cr (VI) oxide	579.5	2.0

Table 3: Fit parameters used for Cr2p3/2

III.1.3. Etching speed calibration

Bilayered (5 and 10 nm) and monolayered (15 nm) Cr and Fe reference samples deposited on a polished 316 stainless steels have been used to calibrate the etching speed (cfr. Experimental section II.1). The evolutions of the carbon, chromium and oxygen contents during the depth profiling of a Cr-based multilayered reference samples are presented in Figure 4. The evolution of the oxygen amount clearly evidences the interface between the two chromium layers as well as between the chromium layer and the stainless steel surface. It should be noted that the deposited chromium is slightly oxidized even inside the layers. This presence of oxygen is due the background vacuum impurities and to the surface oxidation of the Cr source for PVD. Additionally, it is possible to distinguish the carbonaceous impurities at the surface of the stainless steel and at the surface of the chromium bilayer forming during exposure to ambient atmosphere.

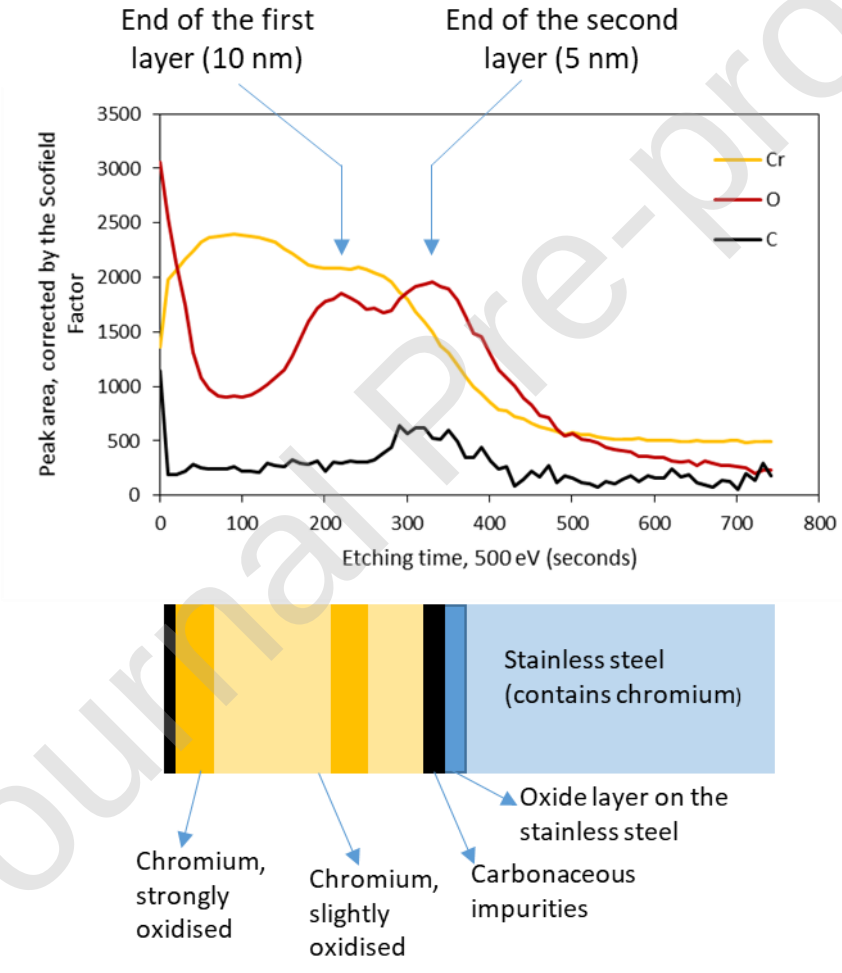

Figure 4: Evolution of the amount of chromium, oxygen and carbon contents during the depth profile XPS analysis and schematic representation of the Cr bilayered standard prepared by PVD onto a stainless steel substrate.

For both Cr and Fe, three different layers of nominally 5 nm, 10 nm and 15 nm have been analyzed by depth profiling in two different locations. Based on the illustration presented here-above, the

sputtering times needed to etch each layer have been identified (the beginning of a new layer is taken as the moment were a maximum oxygen content is detected, see arrows on figure 4). A linear relationship between layer thickness and etching time is observed (Figure 5) and the etching speed can be deduced from the slope. The etching speed of iron is slightly higher than that of chromium (0.051 nm s^{-1} vs. 0.045 nm s^{-1}).

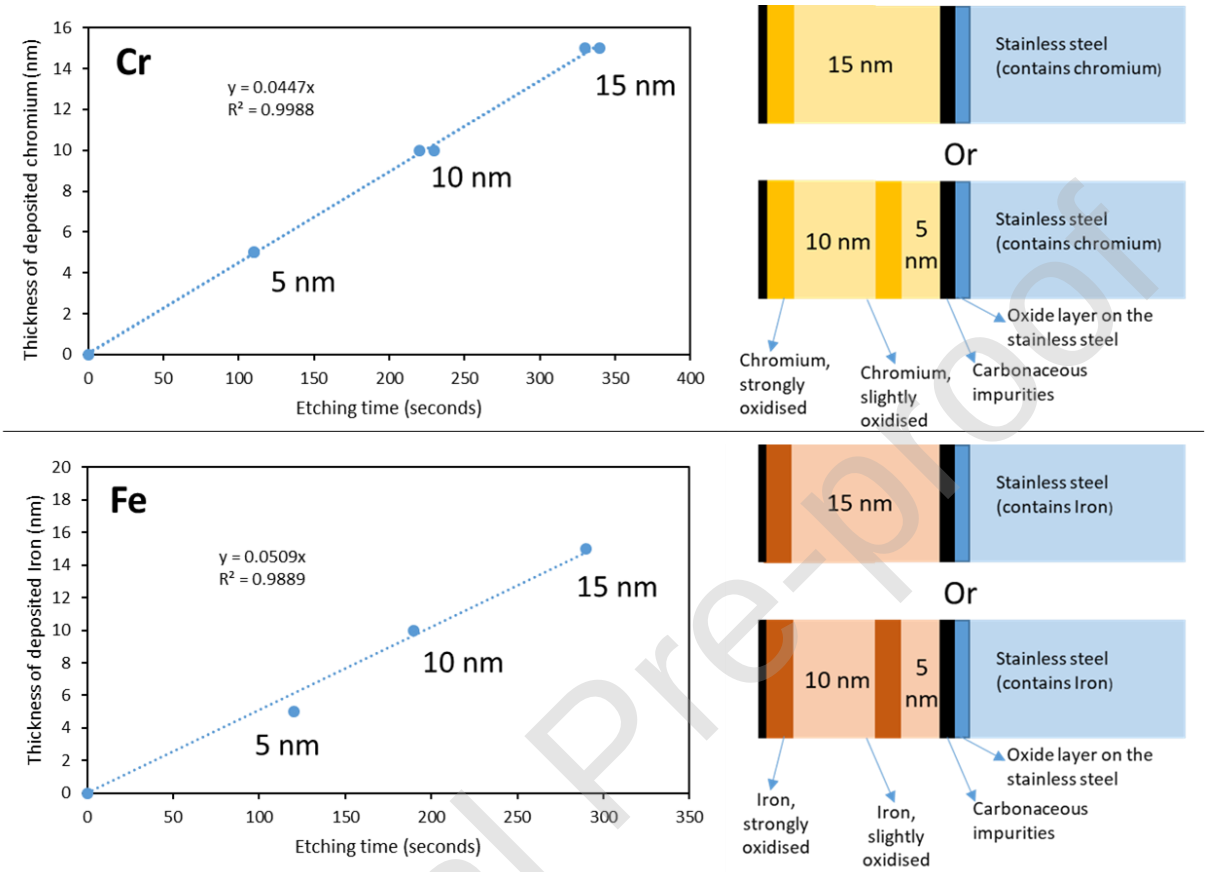

Figure 5: Calibration curve for the etching speed of chromium and iron

III.2. Analysis of the native oxide layer

An analysis methodology will be established using AISI 430 stainless steel (Section III.2.1.). This methodology will then be applied to the cases of AISI 304 and 316 (Section III.2.2.).

III.2.1. Analysis methodology set-up on AISI 430

The analysis methodology is first applied to AISI 430, the less complex of the studied stainless steel grades. The parameters for the depth profiling are identical to those used for the calibration of the etching speed (section III.1.). According to the calibration, 60 etching steps (30 steps of 2 seconds of etching and 40 steps of 4 seconds of etching, corresponding to a total of 180 seconds etching time) are needed to achieve a 6 nm depth. Figure 6, first row, shows the evolution of the amount of carbon, oxygen, iron and chromium as a function of the etching depth for AISI 430. The data obtained from the

various depth profiles of AISI 430 are reproducible. A superposition of the various depth profiles is presented in the figure 1 of supporting information (S.I. 1). XPS spectra for iron, chromium, nickel and molybdenum corresponding to characteristic points of the depth profile are shown in S.I. 2.

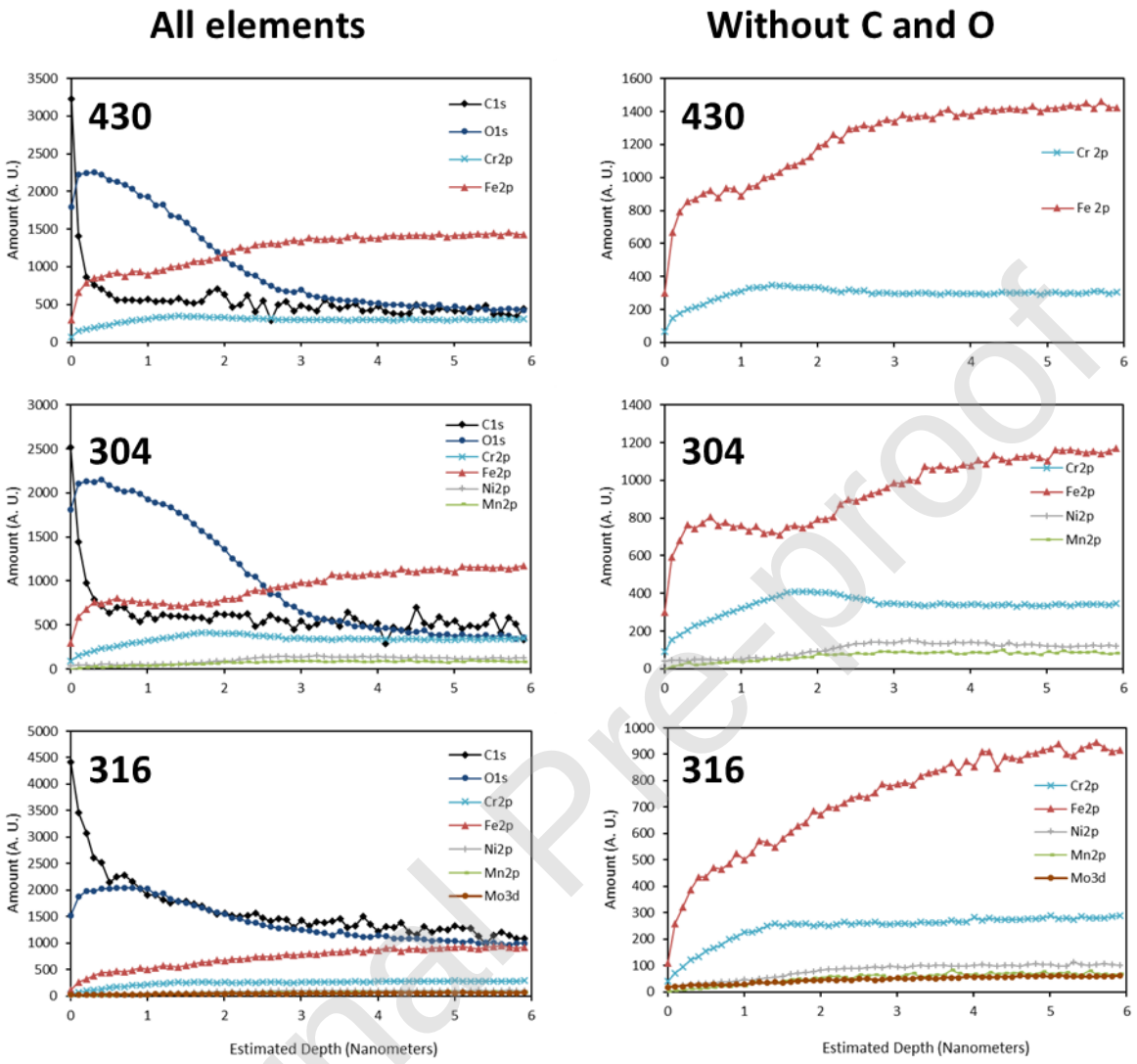

Figure 6: Evolution of carbon, oxygen, iron, chromium, nickel and molybdenum amounts during depth profiling on as-provided AISI 430, AISI 304, and AISI 316 stainless steels.

The depth profile shows the presence of carbon and oxygen throughout the analyzed depth. The oxide layer is characterized by an accumulation of chromium, which is located at a depth ranging from 1 to 2 nm. The chromium accumulation is concomitant with a decrease of the iron content. This observation is consistent with the higher diffusion rate of iron ions comparatively to chromium ions during the formation of the oxide layer [18,38]. The bulk theoretical composition is reached at a depth of 3 to 3.5 nm.

Using the tables with fitting parameters for iron and chromium presented in section III.1., the signal evolution of the oxide, hydroxide and metallic components of chromium and iron as a function of the

etching depth is determined (figure 7). The amount of oxygen determined via the O1s peak or the metal oxide peaks (taking into account their stoichiometry) matches, which confirm the reliability of fitting parameters (see supporting information, figure 3).

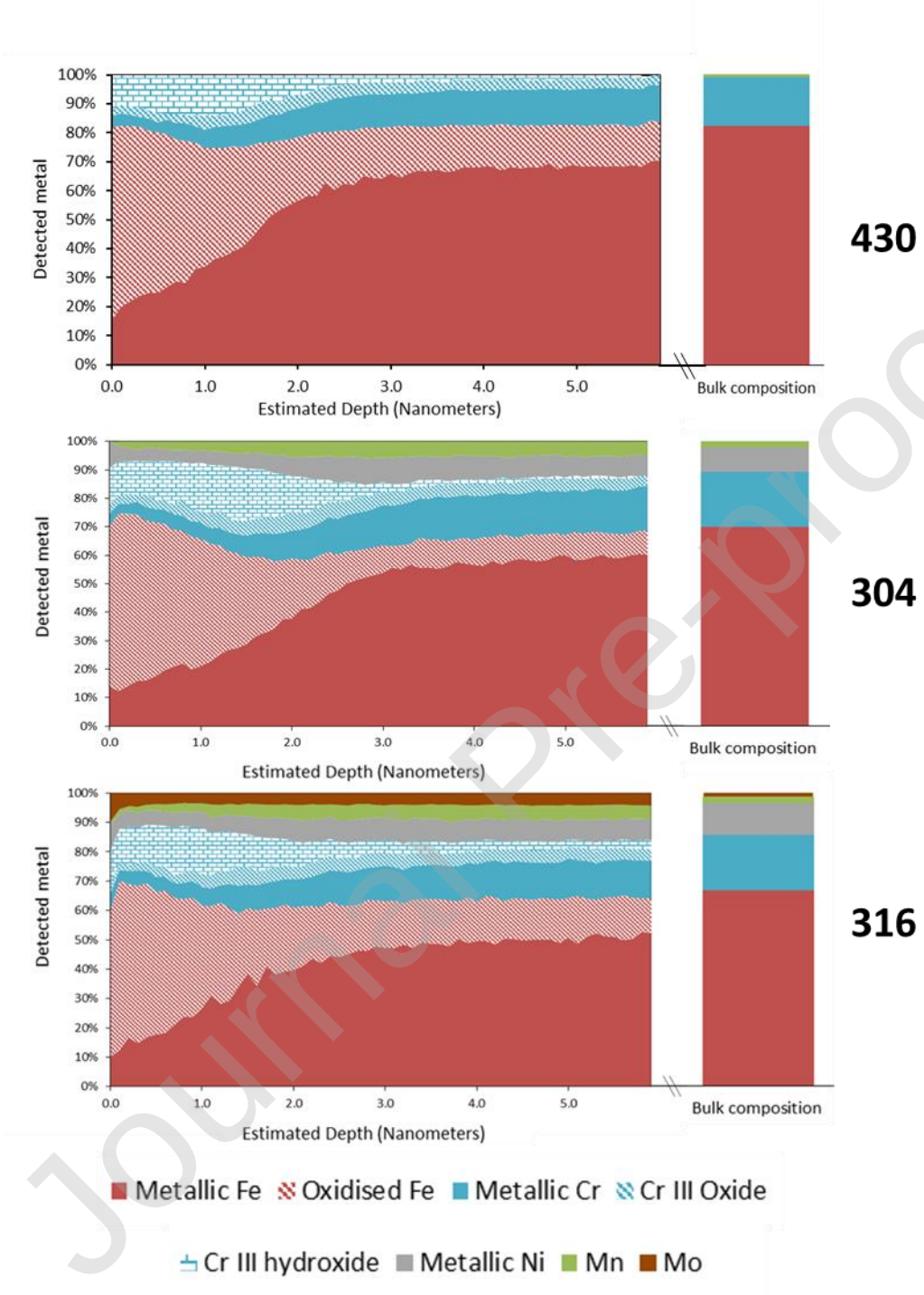

Figure 7: Evolution of the various oxides, hydroxides and metallic components of iron and chromium as a function of etching depth (left) and theoretical bulk composition (right) for AISI 430, 304 and 316 samples

Figure 7 shows that the oxide layer is composed of iron mainly in the form of iron oxides (Fe_2O_3 and Fe_3O_4) and chromium mainly in the form of hydroxide. The signals of non-oxidized chromium and iron

observed at the beginning of the depth profile (2 nanometers) originate from the underlying metallic bulk. Most of the oxidized iron (taking into account the amount of oxidized iron masked by the roughness) has disappeared at a depth of 2 to 2.5 nm. The oxidized forms of chromium follow the same trend. From these observations, it can be concluded that the oxide layer has a thickness of roughly 2 to 2.5 nm even if the theoretical bulk composition is only reached at a depth of 3.5 nm. The layer of constant composition in iron laying between the surface and a depth of 2 nm is made of oxidized iron.

Based on these observations, it appears that the underlying material is covered by a chromium hydroxide rich layer (1 to 1.5 nm thick), itself covered by a 1 nm thick layer of iron oxide.

Figure 8 shows the oxide layer thickness by applying the Strohmeier formula (section II.5) to iron and chromium AISI 430 depth profiles. (reproducibility is shown in S.I. 4).

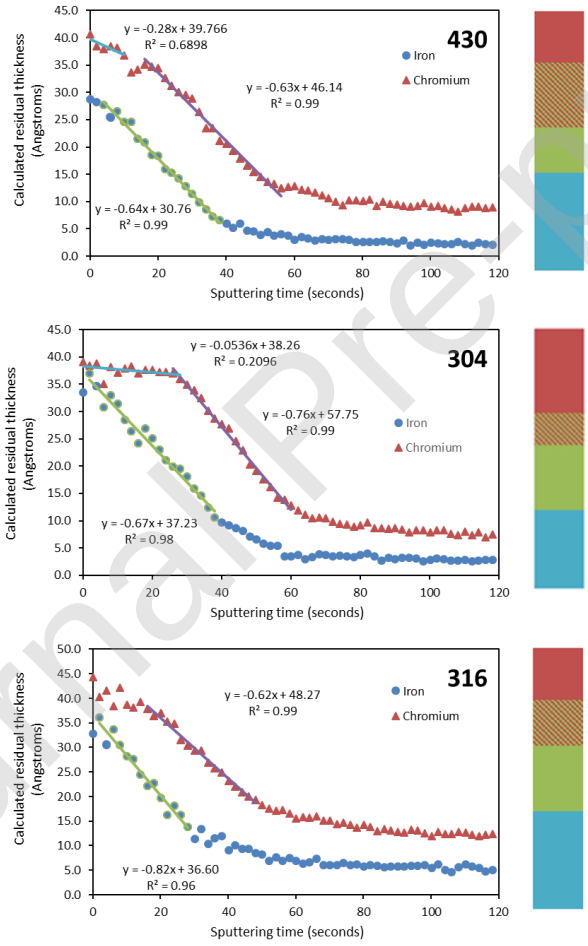

Figure 8: The calculated oxide layer thickness (using the Strohmeier relation) as a function of the etching time and the corresponding proposed structure for the oxide layer (Iron oxide in red, mixed iron and chromium oxide in hatched color, rich in chromium oxide in green and bulk composition in blue)

In the case of the iron signal, the decrease of the calculated residual thickness (δ_{calc}) starts from the first step of etching (2 seconds). A linear decrease of δ_{calc} obtained from the chromium signal is also observed but only starting from the ninth step (18 seconds).

These observations can be accounted by a layered structure of the oxide (Fig.8). The first etched layer is only composed of iron oxide. After 18 seconds (9 levels of 2 seconds), a layer containing also chromium is etched. This layer also contains iron oxide as δ_{calc} calculated from iron still decreases. After 40 seconds of etching, δ_{calc} obtained from the iron spectrum reaches a minimum. This implies that there is no more iron oxide left. However, δ_{calc} from the chromium peak continues to decrease suggesting that there is still chromium oxide. This points the presence of a trilayer structure: the first layer contains only iron oxide, the second one a mixture of iron and chromium oxides and the third layer only chromium oxide. The calculated residual oxide thickness decreases linearly for both metals, which means that iron and chromium oxides have a constant concentration in all layers.

III.2.2. Application of the methodology to AISI 304 and 316

The methodology established on the AISI 430 stainless steel has been applied to AISI 304 and AISI 316 steels of more complex composition. The depth profiles are obtained using the same conditions as described in section III.1. Figure 7 shows the evolution of the amount of the various elements during the depth profiling. The reproducibility of the approach is provided in the supporting information section (figure SI5).

As seen in the case of AISI 430, the amount of carbon and oxygen monitored throughout the profiling can be attributed to contributions from the edge of the sputtering site or due to the roughness. For AISI 304, an accumulation of chromium is observed in a 1.5 to 2.5 nm depth range. This accumulation is higher than the one detected for AISI 430. In the case of AISI 304, a second accumulation layer, richer in nickel, is detected in a 2.5 to 3.5 nm depth range. The bulk composition is reached at a depth of 4 nm. Using the tables with fitting parameters presented in section III.1, figure 7 shows the evolution of the oxide, hydroxide and metallic components of chromium and iron as a function of the etching depth. The reliability of the fitting parameters can be assessed by the correspondence between the oxygen detected on the O1s spectra and the oxygen amount obtained from the oxide components of the respective metal peaks and the corresponding oxide or hydroxide stoichiometry (SI figure 6). Unlike chromium and iron, nickel appears only in its metallic form (cfr. SI figure 7).

For AISI 316, the amount of chromium in the oxide layer does not increase as for AISI 430 and AISI 304 steels. The iron depletion, also visible for AISI 430 and AISI 304, is observed and the Cr/Fe ratio increases in the 1.3 to 2.5 nm depth range. An upper oxide layer, with a higher iron content is observed from 0.3 to 1.3 nm. Finally, the upper layer is enriched in molybdenum at the expense of iron (figure 7). Unlike what has been observed for AISI 304, no nickel accumulation is observed before reaching the bulk composition. The bulk composition is reached at a depth of around 3.5 to 4.0 nm. However,

the region between 2.5 and 4 nm appears more like a “transition region” probably due to the high roughness of the sample.

The reliability of the fitting parameters is again confirmed by comparison between the amount of oxygen determined from the O1s peak and the amount of oxygen estimated from the oxide amount and stoichiometry (see Supporting Information, figure 6).

Figure 8 shows the evolution of δ_{calc} as a function of the etching time using the Strohmeier equation. As in the case of AISI 430, the oxide layer of AISI 304 presents a trilayer structure: a first layer composed of pure iron oxide, a transition layer including iron oxide and chromium oxide/hydroxide and a third layer rich in chromium oxide. The main differences with AISI 430 are the fact that the first layer is thicker and the third layer still contains some iron oxide.

As for AISI430, AISI 316 shows a trilayer strcture of the oxide layer.

For both steels, the absence of nickel oxide makes impossible the use of the Strohmeier equation for this element.

III.2.3. Oxide layer structure

From the above analyses, the oxide layer structure for the three steels can be established as illustrated in figure 9.

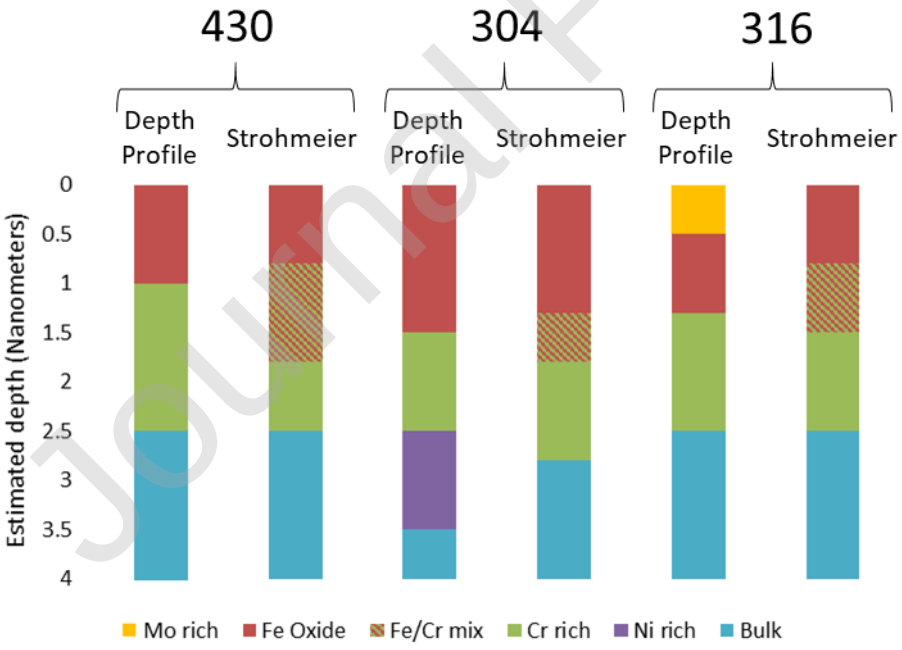

Figure 9: Oxide layer structure of as-provided stainless steels deduced form the depth profile or from the use of the Strohmeier relation for AISI 430, 304 and 316.

From the above results, the application of a fast depth profiling appears to be an efficient method to determine the oxide layer structures. The structures obtained using two different methods of analysis are coherent and compatible with what is reported in the literature [5-24].

In the case of the 430 grade, a trilayer structure is observed with (i) an outer layer of iron oxide, an intermediate layer consisting in a mixture of chromium hydroxide and iron oxide and finally a chromium-rich layer. A similar structure is observed for the 304 grade with an additional, nickel-rich, layer between the chromium-rich one and the bulk. The oxide layer structures for those two stainless steel grades are similar to those reported in the literature with the additional observation of a trilayered structure as suggested in the literature [18,39,40].

The as-received AISI 316 grade is characterized by the absence of an accumulation of metallic nickel as reported by Mandrino *et al* [26]. Moreover, a molybdenum oxide rich layer is clearly detected at the surface of the sample, a feature that is not reported in the literature.

III.3. Analysis of modified fresh native oxides layer

III.3.1. Influence of mechanical polishing

Directly after mirror-like mechanical polishing, the three stainless steels grades were analyzed using the same etching conditions as described in section III.1. For each stainless steel, two analyses were carried out on two different samples. The obtained depth profiles are well reproducible (SI, figure 8). The elemental distributions (metal, oxide or hydroxide) and the evolution of δ_{calc} are presented in Figure 10 for the mechanically polished AISI 430, 304 and 316 steels.

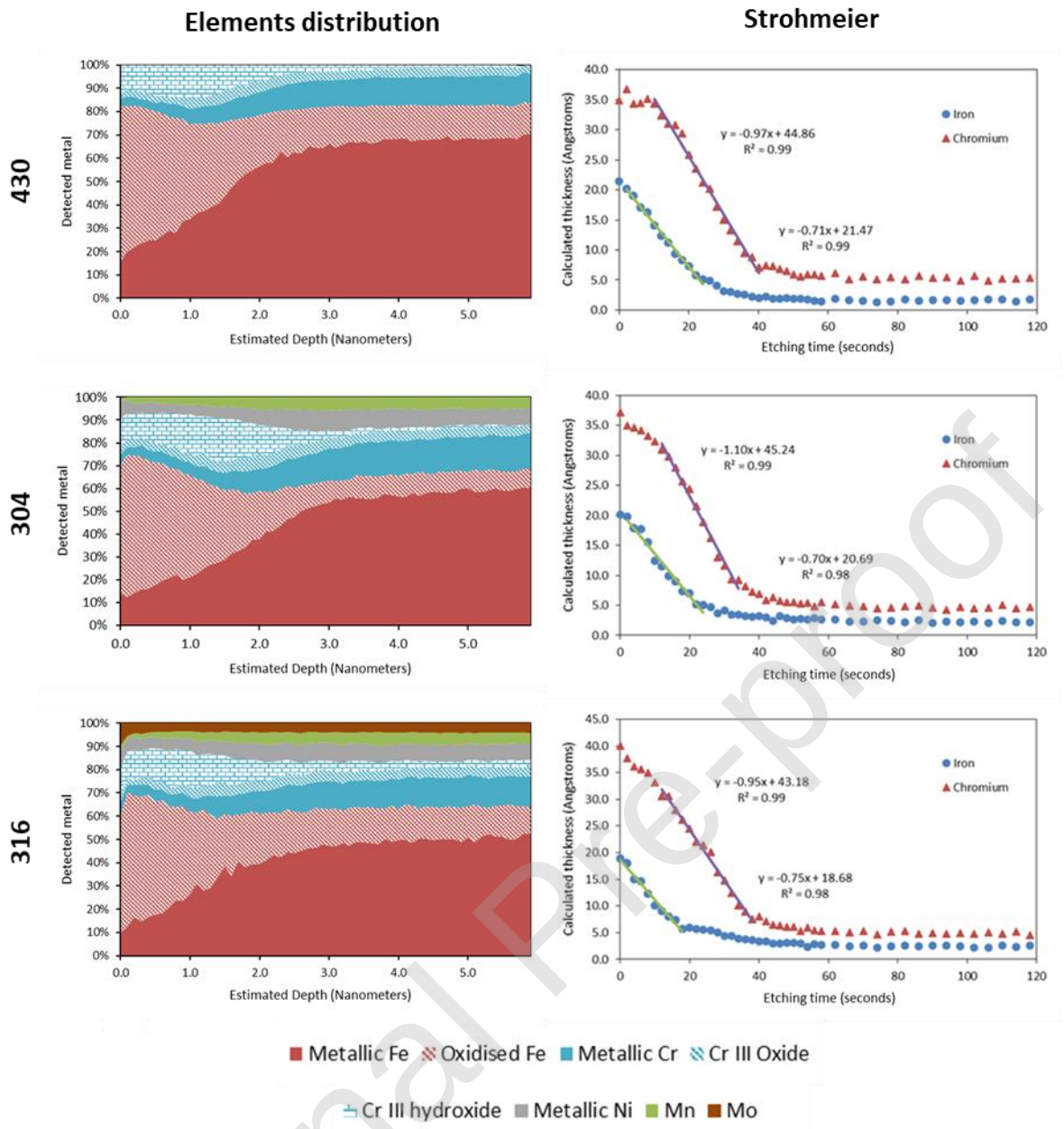

Figure 10: Elements distribution (left) and the evolution of δ_{calc} (Strohmeier relation) (right), as a function of depth for the three stainless steels.

These data were analyzed using the methodology described in section III.2. in order to establish a structure for the oxide layer of each mechanically polished stainless steel. Both methods provide interesting and complementary insights on the oxide layer structure. To assess the impact of mechanical polishing on the oxide structure, the oxide layers structures of mechanically polished *vs.* bare stainless steels are compared in Figure 11.

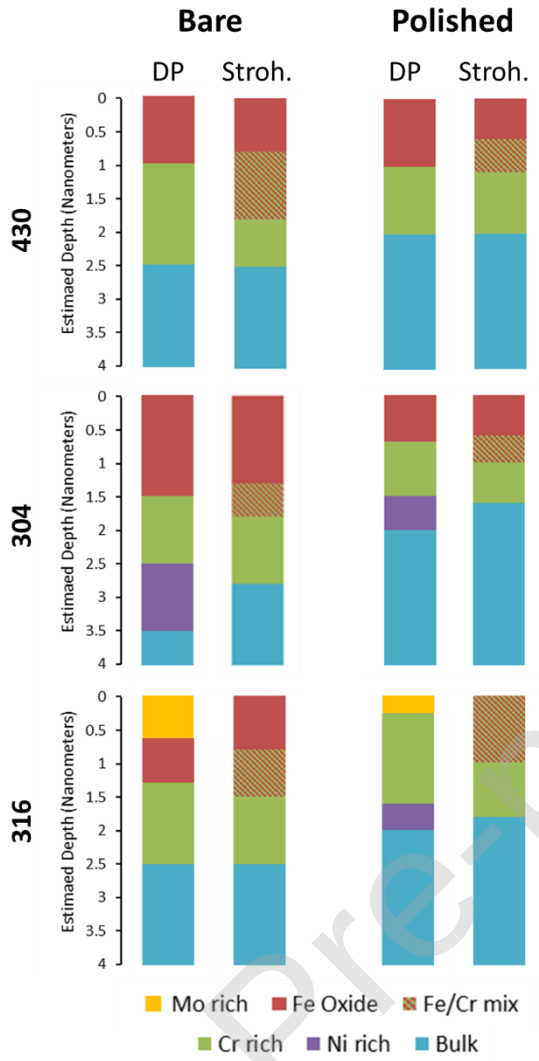

Figure 11: Comparison of the obtained structure from depth profiling (DP) and Strohmeier (Stroh.) analyses for the oxide layer on as received and polished AISI 430, AISI 304 and AISI 316 stainless steels.

For AISI 304 and AISI 430, mechanical polishing leads to a decrease of the oxide layer thickness and a conservation of the trilayered structure. The decrease of the oxide thickness is larger for AISI 304 than for AISI 430 and AISI 316. For the three stainless steels, the accumulation of chromium is more important after polishing. The chromium oxide has the same thickness after mechanical polishing, but the slope of the linear range of the Strohmeier relation indicates a higher concentration in chromium. For AISI 304, the mechanical polishing leads to a thinner nickel layer. In the case of AISI 316, no pure iron layer is found at the surface and an accumulation of metallic nickel is detected just beneath the oxide layer after mechanical polishing.

As a conclusion, for the three steels the mechanical polishing produces an oxide layer thinner than the native one. In term of individual elements, the mechanical polishing decreases the iron oxide layer thickness for AISI 430 and 304. This iron oxide layer is not anymore present in the case of AISI 316. The composition of the chromium oxide rich layer increases.

In the case of steels containing nickel (AISI 304 and 316), the mechanical polishing produces a metallic nickel enriched layer beneath the oxide layer.

III.3.2. Evolution of the oxide layer with aging time

In order to determine the influence of the aging time on the oxide structure, the three stainless steels have been analyzed using depth profiling after mirror-like mechanical polishing and various durations (0, 24, 48, 72, 210, 384 and 624 hours) of contact with the atmosphere. For each condition, two samples have been analyzed and the mean value of the parameters are considered.

Two parameters have been defined. The first one is the etching time needed to attain the beginning of the element (chromium and nickel) accumulation. It corresponds to the maximum of the XPS signal intensity for this element. The second one is the depth at which the bulk composition (+/- 10% [41,42]) of the element is reached.

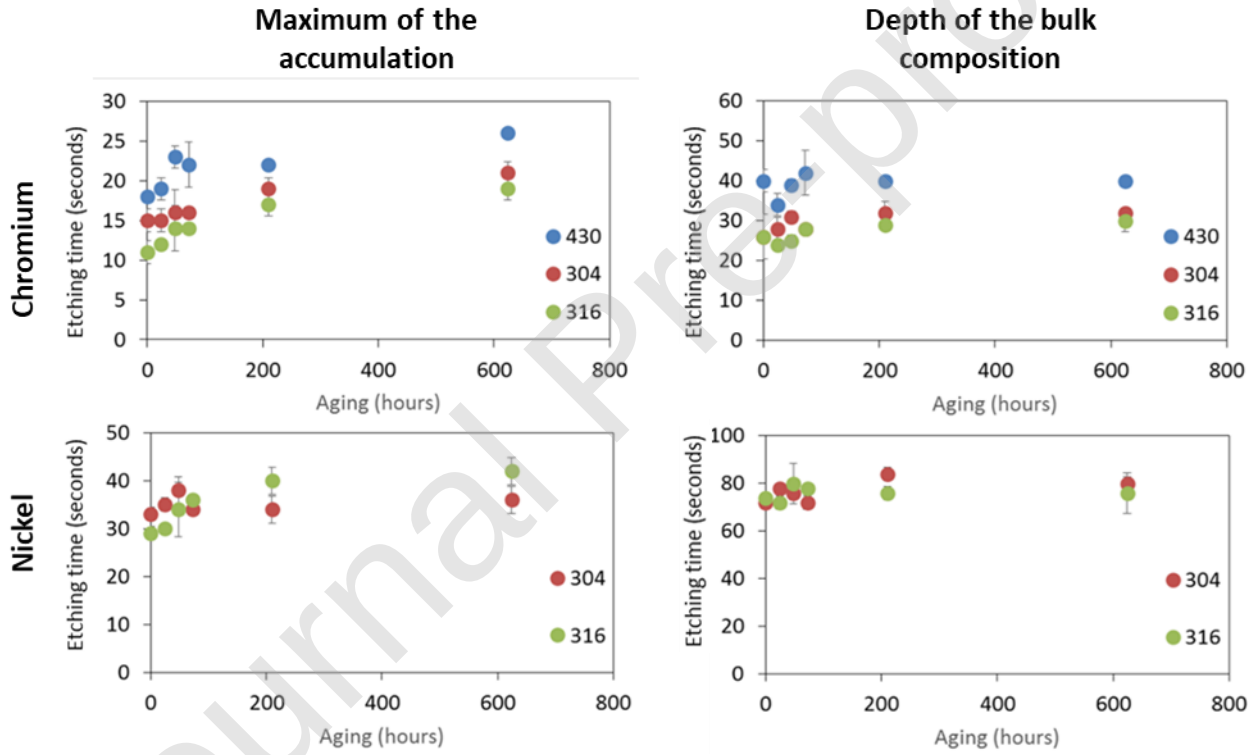

Figure 12: Etching time to reach the maximum of accumulation and the bulk composition for chromium and nickel as a function of aging time for the three steels.

The etching time to reach the accumulation maximum increases with aging time for all elements. On the other hand, the etching time to reach the bulk composition remain stable. This can be due to the diffusion of chromium or nickel inside the oxide layer from the accumulation layers towards the surface.

The measured amount of chromium (or nickel) during the etching is observed to follow a sigmoid curve as expected for the etching of a bilayered material [42]. The evolution of the chromium layer of AISI 430 has been plotted for various aging time (Figure 13C). A similar sigmoid evolution is also visible for the iron and nickel layers (Figure 13B and 13 D) and for the interface between the oxygen containing layers and the bulk (Figure 13A).

These observations confirm the evolution of the interface composition by a slow diffusion process. The aging time induces a slow modification of the oxide layer structure, by diffusion to the surface or the neighbor layer. This is consistent with statements reported by Asami on AISI 304 and 316 [8], where the oxide thickness slightly increases even at long storage time.

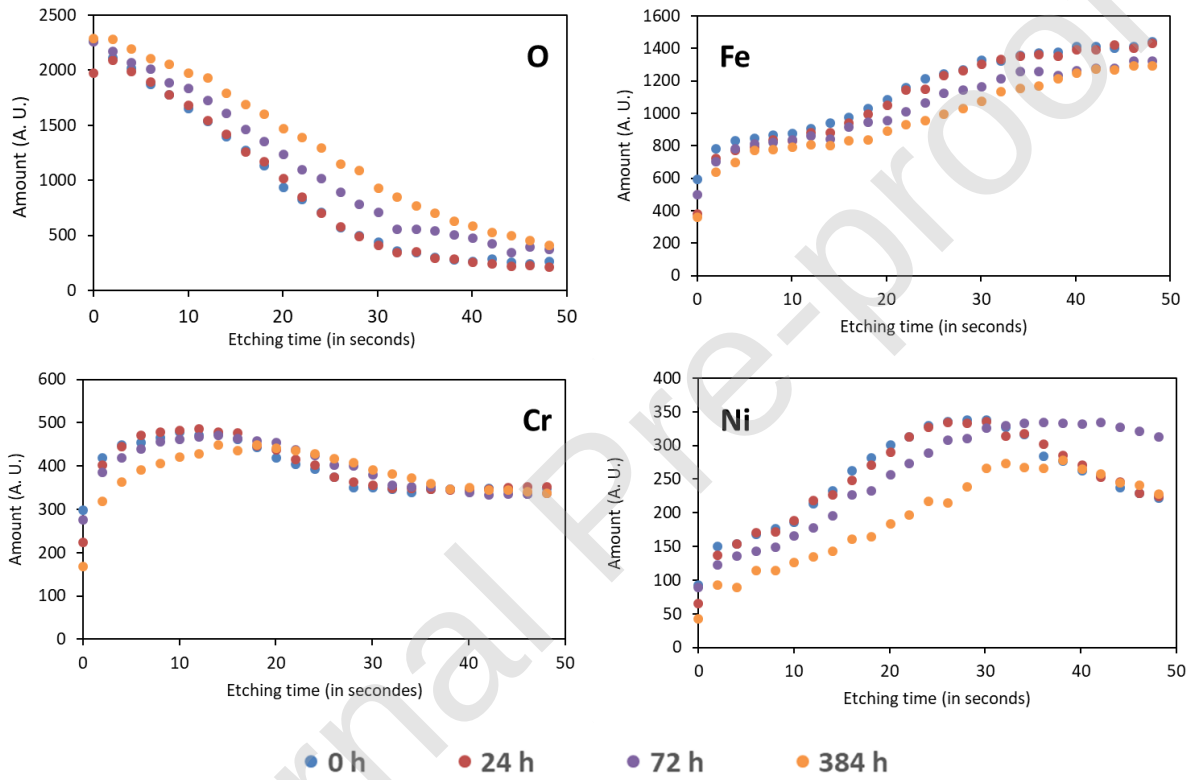

Figure 13: Evolution of the amount of detected chromium, iron and oxygen at the interface between two oxide layers and between the oxide layer and the bulk.

III.4. Confirmation using non-destructive methods

III.4.1. AR-XPS

Using the mirror-like polished samples, AR-XPS has been used in order to confirm the oxide layer structure. Prior to the measurement, a soft etching with Ar^+ at low energy (500 eV) on a large sputtering area (4 mm^2) has been used in order to remove most of the carbonaceous impurities without damaging the oxide layer. Survey spectra of 430 stainless steel before and after the carbonaceous impurities etching are displayed in figure 14 with emphasis on the carbon signal evolution (inset). The same

procedure has been performed on 304 and 316 stainless steel (316 shown in SI, figure 9). AR-XPS measurements have been realized at 20 different angles between 0.0 and 80.0 degrees (4.2 degrees increase) in a snapshot mode with the same acquisition parameters than for depth profiling.

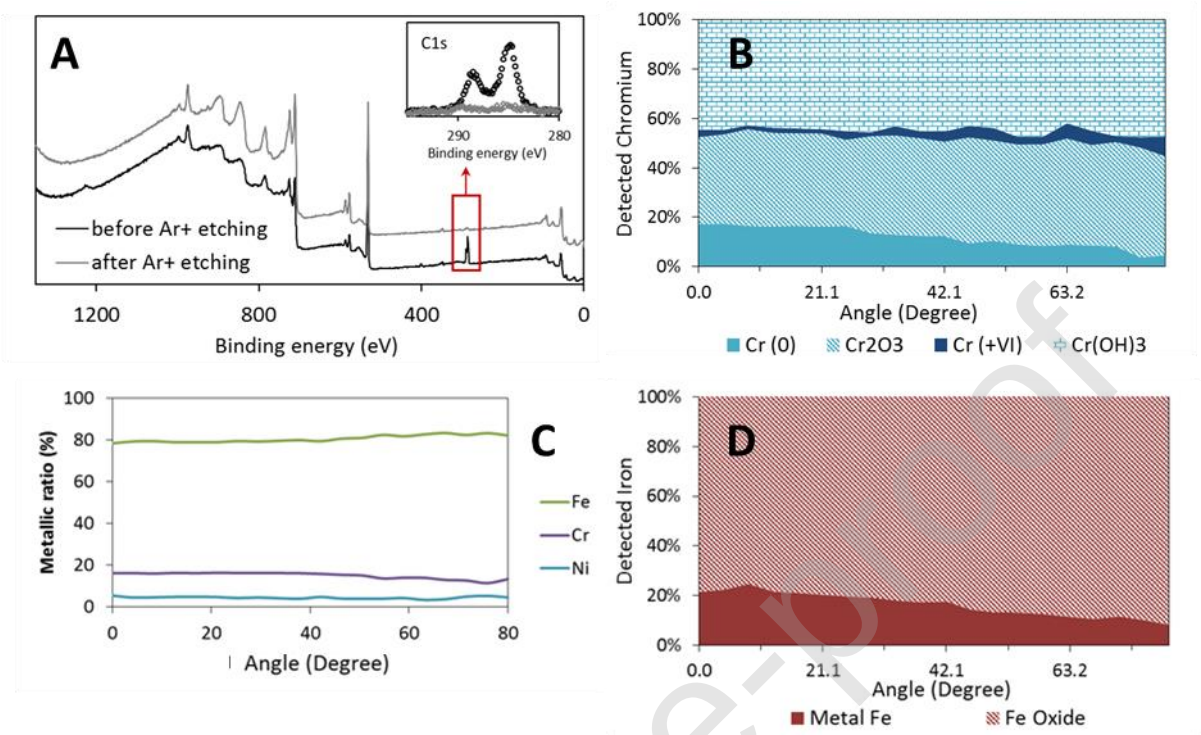

Figure 14: Survey and carbon spectra for 430 stainless steel before and after soft etching of the surface in order to remove carbonaceous impurities (top of right column). Evolution of the atomic ratio and contributions of the various components for chromium and iron for 304 stainless steel.

Analyses of the AR-XPS data have been performed based on the fitting parameters described before (Section III.1) for chromium and iron. The atomic ratios for metals have been plotted as a function of the rotation angle (figure 14).

The AR-XPS analyses confirm most of the observations recorded using the depth profile analyses. The three stainless steels show an extreme surface enriched in iron and poor in chromium. The evolution of the various components of iron and chromium with rotation angle shows the presence of more oxidized forms of both metals close to the surface. Chromium VI, which is almost not detected by depth profile, is barely present and essentially related to the high angle values. The amount of nickel also decreases significantly at high angles for 304 and 316 stainless steels. For 316 steel, the decrease of nickel appears at lower angles than the decrease of chromium. These observations confirm a structure where the bulk is covered by a layer rich in chromium but poor in nickel, itself covered by a layer rich in iron and poor in chromium. There is no clear evidence of molybdenum accumulation on the AR-XPS

data for 316 stainless steel but the molybdenum spectra shows a strong oxidized component at higher angular value (SI, figure 10).

III.4.2. HAXPES

HAXPES measurements have been performed on the three mirror polished stainless steels (aged 6 days) using 2.300 and 6.900 keV X-Ray energies. The analysis focuses on the high-resolution spectra of the various components of the stainless steels, as well as on the carbon and oxygen signals. The atomic percentages of each element have been calculated on the basis of the area under the peaks and the Scofield factors. In order to get rid of the influence of the amount of carbonaceous impurities, for each element of the stainless steel, ratios between the atomic percentage of the element and the sum of all the metallic elements have been used. A comparison of those ratios for the three X-Ray energy (1.487 keV from XPS, 2.300 and 6.900 keV from HAXPES) and the bulk theoretical composition is presented in tables 4, 5 and 6.

	XPS	HAXPES		
Ratio	1.487 keV	2.300 keV	6.900 keV	Bulk
Cr/(Cr+Fe)	0.169 ± 0.0067	0.258 ± 0.0076	0.200 ± 0.0070	0.173
Fe/(Cr+Fe)	0.831 ± 0.013	0.741 ± 0.012	0.800 ± 0.013	0.827

Table 4: Chromium and iron ratio for AISI 430 at the various investigated X-Ray energies

For AISI 430, by increasing the X-Ray energy from 1.487 keV to 2.300 keV, an increase of the detected ratio of chromium is observed. A further increase of the X-Ray energy leads to a decrease of the chromium ratio to values close to the bulk composition. An opposite evolution is observed for the iron ratio. This can be interpreted as follows: (i) at 1.487 keV X-Ray energy, most of the signal comes from an outer layer, rich in iron and poor in chromium. (ii) At a higher X-Ray energy (2.300 keV), a larger fraction of the signal originates from a deeper layer richer in chromium, and (iii) at 6.900 keV X-Ray energy, most of the signal comes from deeper layers close to the bulk composition. This observation is consistent with a structuration of the oxide layer made out of (i) an iron oxide rich layer, followed by (ii) a chromium oxide rich one and then (iii) the bulk. This structure matches with the one obtained from the XPS depth profile and AR-XPS data. Using the TPP2M equation [43], the electron mean free path for the three energies used are calculated: (i) ± 1.5 nm for 1.487 keV, (ii) ± 2.5 nm for 2.300 keV and (iii) ± 7.0 nm for 6.900 keV. The calculation have been performed considering a pure metal (chromium and iron) or a pure oxide layer. The results differs depending on the considered nature of the layer. As an example, values goes from 2.3 to 2.7 nm for 2.300 keV. Using these values, the depth of the chromium-rich layer is located at around 2.5 nm (at least higher than 1.5 nm), which is consistent with the estimated depth of this layer obtained from the depth profile.

	XPS	HAXPES		
Element	1.487 keV	2.300 keV	6.900 keV	Bulk
Cr/(Fe+Cr+Ni)	0.191 ± 0.0079	0.284 ± 0.0093	0.213 ± 0.0082	0.190
Fe/(Fe+Cr+Ni)	0.745 ± 0.016	0.604 ± 0.014	0.576 ± 0.014	0.716
Ni/(Fe+Cr+Ni)	0.011 ± 0.0052	0.112 ± 0.0067	0.191 ± 0.0079	0.084

Table 5: Ratios of the metallic elements at the various investigated X-Ray energies for AISI 304

	XPS	HAXPES		
Element	1.487 keV	2.300 keV	6.900 keV	Bulk
Cr/(Fe+Cr+Ni+Mo)	0.191 ± 0.0088	0.227 ± 0.0095	0.167 ± 0.0083	0.185
Fe/(Fe+Cr+Ni+Mo)	0.706 ± 0.019	0.624 ± 0.017	0.621 ± 0.017	0.677
Ni/(Fe+Cr+Ni+Mo)	0.054 ± 0.0061	0.141 ± 0.0078	0.181 ± 0.0086	0.110
Mo/(Fe+Cr+Ni+Mo)	0.039 ± 0.0058	0.000 ± 0.0050	0.019 ± 0.0054	0.013

Table 6: Ratios of the metallic elements at the various investigated X-Ray energies for AISI316

For both AISI 304 and 316 alloys, the chromium and iron ratio evolution is similar to the one observed for AISI 430. The evolution of nickel ratio is the same for both steels but differs from the chromium ratio evolution. When increasing the X-Ray energy from 1.487 to 6.900 keV, the nickel ratio continuously increases. This is due to a layer of nickel accumulation, with a higher nickel ratio than the bulk. In addition, this Ni rich layer is deeper than the one rich in chromium. For both steels, those observations indicate an oxide layer structure consisting in (i) an outer layer rich in iron oxide, (ii) an inner layer richer in chromium oxide and (iii) a deeper layer richer in nickel. This structure is consistent with the one proposed based on the depth profile data. For AISI 316, the evolution of the molybdenum ratio as a function of X-Ray energy points to an accumulation of molybdenum oxide at the extreme surface of the sample. This is also consistent with the depth profile observation of an outer layer richer in molybdenum.

Figure 15 shows the HAXPES spectra for nickel at 2.300 and 6.900 keV energies. The detection of nickel as Ni(0) in HAXPES supports the XPS depth profile results, proving that Ni(0) is not a consequence of a possible reduction during the etching process [44].

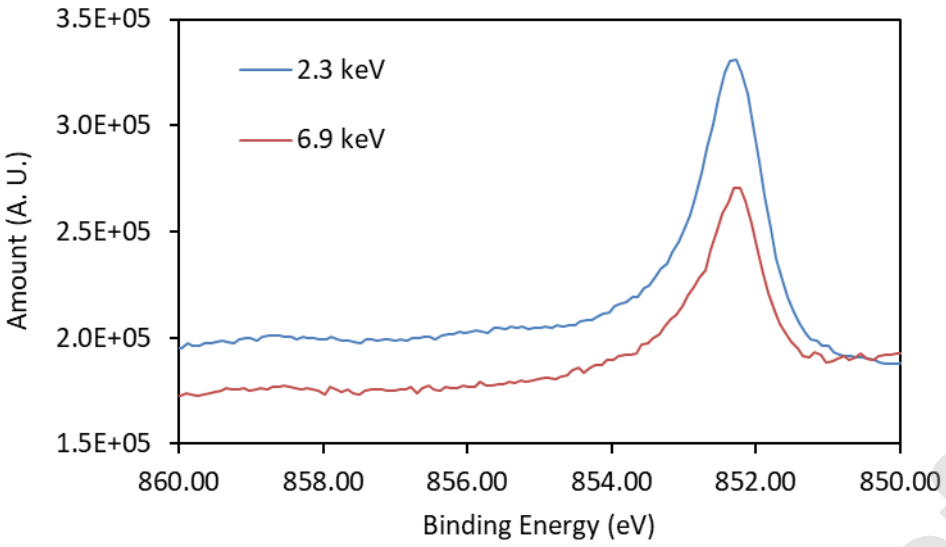

Figure 15: Nickel 2p3/2 high-resolution HAXPES spectra at the two investigated X-Ray energies

IV. Conclusions

In this work, a protocol for fast depth profiling of thin metal oxide layers using a snapshot acquisition is developed. This methodology, applied to three stainless steel grades (AISI 316, 304 and 430, as received and mirror polished), provides a fast, simple and reliable determination of their oxide layer structures. Moreover, the Strohmeier equation, originally applied to the determination of oxide layer thickness, is used as a powerful tool for the determination of the oxide layer structures. The validity of the structures obtained from XPS depth profiling is confirmed using two non-destructive techniques, AR-XPS and HAXPES.

The three studied stainless steel grades present a three level oxide layer structuration. The surface layer, composed essentially of iron oxide, is followed by a mixed layer of chromium and iron oxide itself followed by a chromium oxide rich layer. This tri-layered structure proposed previously in the literature (ToF-SIMS, theoretical approaches) finds confirmation in the present study by using a rapid (snapshot) XPS depth profiling.

For the stainless steels containing nickel (AISI 304 and 316), an accumulation of metallic nickel at the interface between the oxide layer and the bulk has been evidenced. For the molybdenum containing grade (AISI 316), a slightly different structure is found, where a molybdenum oxide rich surface layer has replaced the iron oxide one.

The aging of the oxide layer in contact with atmosphere (624 hours) has also been studied. It appears that the thin oxide layer and its structure evolve during aging within the first 300 hours and afterward stabilize. The observed changes are in line with the assumption of ions or atoms diffusion from the accumulated buried layers of chromium and nickel towards the surface.

V. Acknowledgment

The authors acknowledge SOLEIL for provision of synchrotron radiation facilities (proposal 20180830) and would like to thank D. Céolin and J.-P. Rueff for assistance in using beamline “GALAXIES”.
The authors thanks the DGO6 for supporting this research in the field of AdEPT project (convention 1610449)

VI. References

[1] N.R. Baddoo, Stainless steel in construction: A review of research, applications, challenges and opportunities, J. Constr. Steel Res. 64 (2008) 1199–1206. doi:10.1016/j.jcsr.2008.07.011.

[2] International Nickel Study Group, Press release, in: Int. Nickel Study Group, Press Release, 2018.

[3] K.H. Lo, C.H. Shek, J.K.L. Lai, Recent developments in stainless steels, Mater. Sci. Eng. R Reports. 65 (2009) 39–104. doi:10.1016/j.mser.2009.03.001.

[4] J.P. Berge, berge.pdf, in: Eur. At. Energy Community Rep. N°1709, n.d.

[5] C.O.A. Olsson, D. Landolt, Passive films on stainless steels - Chemistry, structure and growth, Electrochim. Acta. 48 (2003) 1093–1104. doi:10.1016/S0013-4686(02)00841-1.

[6] R.P. Frankenthal, D.J. Siconolfi, Quantitative composition-depth profiles of thin films, Surf. Interface Anal. 7 (1985) 223–227. doi:10.1002/sia.740070505.

[7] B.M. Seo, N. Sato, Surface Characterization of Stainless Steels Prepared with Various Surface Treatments, Trans. Japan Inst. Met. 21 (1980) 805–810.

[8] K. Asami, K. Hashimoto, an X-Ray Photo-Electron Spectroscopic Study of Surface Treatments of Stainless Steels, Corros. Sci. 19 (1979) 1007–1017.

[9] K. Asami, K. Hashimoto, An XPS study of the surfaces on Fe-Cr, Fe-Co and Fe-Ni alloys after mechanical polishing, Corros. Sci. 24 (1984) 83–97. doi:10.1016/0010-938X(84)90039-8.

[10] S. Haupt, H.H. Strehblow, A combined surface analytical and electrochemical study of the formation of passive layers on Fe Cr alloys in 0.5 M H2SO4, Corros. Sci. 37 (1995) 43–54. doi:10.1016/0010-938X(94)00104-E.

[11] R.H. Jung, H. Tsuchiya, S. Fujimoto, XPS characterization of passive films formed on Type 304 stainless steel in humid atmosphere, Corros. Sci. 58 (2012) 62–68. doi:10.1016/j.corsci.2012.01.006.

[12] K. Hashimoto, K. Asami, K. Teramoto, An X-ray photo-electron spectroscopic study on the role of molybdenum in increasing the corrosion resistance of ferritic stainless steels in HC1, Corros. Sci. 19 (1979) 3–14. doi:10.1016/0010-938X(79)90003-9.

[13] C.M. Abreu, M.J. Cristóbal, R. Losada, X.R. Nóvoa, G. Pena, M.C. Pérez, The effect of Ni in the electrochemical properties of oxide layers grown on stainless steels, Electrochim. Acta. 51 (2006) 2991–3000. doi:10.1016/j.electacta.2005.08.033.

[14] W. Fredriksson, S. Malmgren, T. Gustafsson, M. Gorgoi, K. Edström, Full depth profile of passive films on 316L stainless steel based on high resolution HAXPES in combination with ARXPS, Appl. Surf. Sci. 258 (2012) 5790–5797. doi:10.1016/j.apsusc.2012.02.099.

[15] M. Lampimäki, K. Lahtonen, P. Jussila, M. Hirsimäki, M. Valden, Morphology and composition of nanoscale surface oxides on Fe–20Cr–18Ni{1 1 1} austenitic stainless steel, J. Electron Spectros. Relat. Phenomena. 154 (2007) 69–78. doi:10.1016/J.ELSPEC.2006.12.002.

[16] C. Calinski, H. -H. Strehblow, ISS Depth Profiles of the Passive Layer on Fe/Cr Alloys, J. Electrochem. Soc. 136 (1989) 1328. doi:10.1149/1.2096915.

[17] K. Asami, K. Hashimoto, S. Shimodaira, XPS determination of compositions of alloy surfaces and surface oxides on mechanically polished iron-chromium alloys, Corros. Sci. 17 (1977) 713–723. doi:10.1016/0010-938X(77)90067-1.

[18] J.R. Lince, S. V. Didziulis, D.K. Shuh, T.D. Durbin, J.A. Yarmoff, Interaction of O2 with the Fe0.84Cr0.16(001) surface studied by photoelectron spectroscopy, Surf. Sci. 277 (1992) 43–63. doi:10.1016/0039-6028(92)90611-9.

[19] A.P. Greeff, C.W. Louw, H.C. Swart, The oxidation of industrial FeCrMo steel, Corros. Sci. 42 (2000) 1725–1740. doi:10.1016/S0010-938X(00)00026-3.

[20] P.D. Han, H.F. Li, X.L. Sun, W. Liang, H.B. Dong, B.S. Xu, Combined first principle and experimental study of oxide/alloy interface evolution during hot rolling 430 stainless steels, Ironmak. Steelmak. 38 (2011) 530–533. doi:10.1179/1743281211Y.0000000032.

[21] G. Betz, G.K. Wehner, L. Toth, A. Joshi, Composition-vs-depth profiles obtained with Auger electron spectroscopy of air-oxidized stainless-steel surfaces, J. Appl. Phys. 45 (1974) 5312–5316. doi:10.1063/1.1663236.

[22] Y. Soma, C. Kato, M. Yamamoto, Growth Behavior of Surface Oxide Layer on SUS316L Stainless Steel at the Early Stage of Exposure to 288 degrees C Water, Mater. Trans. 53 (2012) 195–200. doi:DOI 10.2320/matertrans.M2011200.

[23] I. Olefjord, B.-O. Elfstrom, The Composition of the Surface during Passivation of Stainless Steels, CORROSION. 38 (1982) 46–52. doi:10.5006/1.3577318.

[24] C.-O.A. Olsson, S. Malmgren, M. Gorgoi, K. Edström, Quantifying the Metal Nickel Enrichment on Stainless Steel, Electrochem. Solid-State Lett. 14 (2011) C1. doi:10.1149/1.3509122.

[25] H.J. Mathieu, D. Landolt, An investigation of thin oxide films thermally grown in situ on Fe24Cr and Fe24Cr11Mo by auger electron spectroscopy and X-ray photoelectron spectroscopy, Corros. Sci. 26 (1986) 547–559. doi:10.1016/0010-938X(86)90022-3.

[26] D. Mandrino, Č. Donik, M. Jenko, AES of thin oxide layers on a duplex stainless steel surface, Surf. Interface Anal. 42 (2010) 762–765. doi:10.1002/sia.3212.

[27] A. Kocijan, Č. Donik, M. Jenko, Electrochemical and XPS studies of the passive film formed on stainless steels in borate buffer and chloride solutions, Corros. Sci. 49 (2007) 2083–2098. doi:10.1016/j.corsci.2006.11.001.

[28] Increased Throughput Using Snapshot Spectra, Thermo Sci. Appl. Note 31009. (n.d.) 1–2.

[29] D.A. Shirley, High-Resolution X-Ray Photoemission Spectrum of the Valence Bands of Gold, Phys. Rev. B. 5 (1972) 4709–4714.

[30] J.P. Rueff, J.M. Ablett, D. Céolin, D. Prieur, T. Moreno, V. Balédent, B. Lassalle-Kaiser, J.E. Rault, M. Simon, A. Shukla, The GALAXIES beamline at the SOLEIL synchrotron: Inelastic X-ray scattering and photoelectron spectroscopy in the hard X-ray range, J. Synchrotron Radiat. 22 (2015) 175–179. doi:10.1107/S160057751402102X.

[31] D. Céolin, J.M. Ablett, D. Prieur, T. Moreno, J.P. Rueff, T. Marchenko, L. Journel, R. Guillemin, B. Pilette, T. Marin, M. Simon, Hard X-ray photoelectron spectroscopy on the GALAXIES

beamline at the SOLEIL synchrotron, J. Electron Spectros. Relat. Phenomena. 190 (2013) 188–192. doi:10.1016/j.elspec.2013.01.006.

[32] B.R. Strohmeier, an Esca Method for Determining the Oxide Thickness on Aluminum-Alloys, Surf. Interface Anal. 15 (1990) 51–56. doi:DOI 10.1002/sia.740150109.

[33] J.F. Moulder, W.F. Stickle, P.E. Sobol, K.D. Bomben, Handbook of X-ray photoelectron spectroscopy: a reference book of standard spectra for identification and interpretation of XPS data, Surf. Interface Anal. (1992) 261. doi:9780962702624.

[34] H.A.E. Hagelin-Weaver, G.B. Hoflund, D.M. Minahan, G.N. Salaita, Electron energy loss spectroscopic investigation of Co metal, CoO, and Co3O4before and after Ar+bombardment, Appl. Surf. Sci. 235 (2004) 420–448. doi:10.1016/j.apsusc.2004.02.062.

[35] N.S. McIntyre, D.G. Zetaruk, X-ray Photoelectron Spectroscopic Studies of Iron Oxides, Anal. Chem. 49 (1977) 1521–1529. doi:10.1021/ac50019a016.

[36] A.P. Grosvenor, B.A. Kobe, M.C. Biesinger, N.S. McIntyre, Investigation of multiplet splitting of Fe 2p XPS spectra and bonding in iron compounds, Surf. Interface Anal. 36 (2004) 1564–1574. doi:10.1002/sia.1984.

[37] M.C. Biesinger, B.P. Payne, A.P. Grosvenor, L.W.M. Lau, A.R. Gerson, R.S.C. Smart, Resolving surface chemical states in XPS analysis of first row transition metals, oxides and hydroxides: Cr, Mn, Fe, Co and Ni, Appl. Surf. Sci. 257 (2011) 2717–2730. doi:10.1016/J.APSUSC.2010.10.051.

[38] G.C. Allen, S.J. Harris, J.A. Jutson, A STUDY OF A NUMBER OF MIXED TRANSITION METAL OXIDE SPINELS USING X-RAY PHOTOELECTRON SPECTROSCOPY, Appl. Surf. Sci. 37 (1989) 111–134.

[39] G.C. Allen, J.M. Dyke, S.J. Harris, A. Morris, A surface study of the oxidation of type 304L stainless steel at 600 K in air, Oxid. Met. 29 (1988) 391–408. doi:10.1007/BF00666841.

[40] A.D. Pelton, H. Schmalzried, J. Sticher, Computer-assisted analysis and calculation of phase diagrams of the FeCrO, FeNiO and CrNiO systems, J. Phys. Chem. Solids. 40 (1979) 1103–1122. doi:10.1016/0022-3697(79)90146-X.

[41] S. Hofmann, Y.S. Han, J.Y. Wang, Depth resolution and preferential sputtering in depth profiling of sharp interfaces, Appl. Surf. Sci. 410 (2017) 354–362. doi:10.1016/j.apsusc.2017.03.110.

[42] H. Viefhaus, K. Hennesen, M. Lucas, E.M. Muller-Lorenz, H.J. Grabke, Ion sputter rates and yields for iron-, chromium- and aluminium oxide layers, Surf. Interface Anal. 21 (1994) 665–672. doi:10.1002/sia.740210911.

[43] S. Tanuma, C.J. Powell, D.R. Penn, Calculations of electron inelastic mean free paths. V. Data for 14 organic compounds over the 50–2000 eV range, Surf. Interface Anal. 21 (1994) 165–176. doi:10.1002/sia.740210302.

[44] K.S. Kim, Nicholas Winograd, SURFACE SCIENCE 43 (1974) 21-280 North-Holland Publishing Co., Surf. Sci. 43 (1974) 625–643.